Supporting Information

Incomplete phase metasurface for wavefront reconstruction

Qiyao Liu[1†], Zhengtong Liu[2†], Xuezhi Ma[1], Jie Deng[1], Chen Zhang[2], Zhenmin Chen[2], Arash Nemati[1], Sui Kit Ng[1], Sergey Gorelik[3], Siew Lang Teo[1], Rong Ji[1], Meng Zhao[1], Leonard Verano Gonzaga[1], Hong Liu[1], Fuyong Yue[2], Shaohua Yu[2], Yu Luo[4], Qian Wang[1]**

[1] *Institute of Materials Research and Engineering, Agency for Science, Technology and Research (A*STAR), 2 Fusionopolis Way, Innovis 08-03, 138634, Singapore*

[2] *Peng Cheng Laboratory, Shenzhen, 518055, P. R. China*

[3] *Singapore Institute of Food and Biotechnology Innovation, Agency for Science, Technology and Research (A*STAR), 2 Fusionopolis Way, Innovis 08-03, 138634, Singapore*

[4] *Centre for OptoElectronics and Biophotonics School of Electrical and Electronic Engineering, Nanyang Technological University, Singapore 639798, Singapore*

[†] *These authors contributed equally to this work.*

*Corresponding authors: * liuzht02@pcl.ac.cn; * wangqian@imre.a-star.edu.sg*

This file includes:

Supplementary Note 1. Optical constants of TiO_2

As one kind of popular candidates for metasurface, dielectric material with transparency windows at visible and infrared wavelengths enable applications such as three-dimensional displays, wearable optics and planar optical systems. In this work, TiO_2 is used as base material and deposited by atomic layer deposition on quartz substrate. The thin film is smooth (see Fig. S1), with a surface roughness much smaller than the wavelength of visible light. Otherwise, high surface roughness introduces extraneous light scattering, which is a significant source of loss.

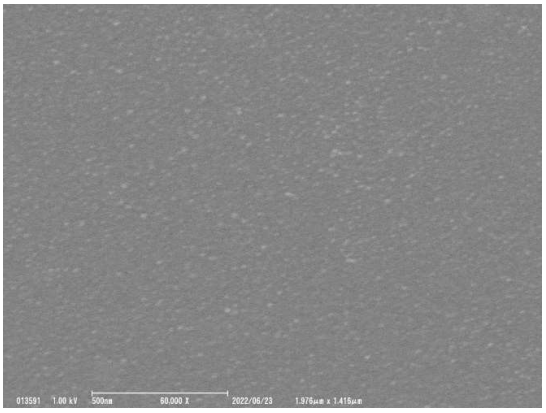

Figure S1. SEM on the surface of TiO_2 thin film

The optical constants of TiO_2 thin film are obtained by ellipsometer (JA Woolam VB400). Here we use the Tauc-Lorentz model to fit and extract the refractive index n and attenuation factor κ. The model we build here is two layers (TiO_2/SiO_2) with surface roughness correction. The thickness of TiO_2 and surface roughness are denoted as Thick.1 and Thick.2. The back reflection factor (BackRef) is also considered. The fit parameters are as follows:

Table S1.

MSE	Thick.1	A	En	BackRef	C	Eg	Thick.2
18.28	155.75±0.147	423.21±63.7	3.6479±0.266	1.5575±0.147	3.8479±0.188	3.33603±0.018	1.978±0.192

where A is amplitude, En is the centre energy, C is broadening, Eg is the bandgap. The overall mean squared error (MSE) is 18.28. Fig. S2b shows the fit graphs. As can be seen at 405nm, n~2.52, κ~0.

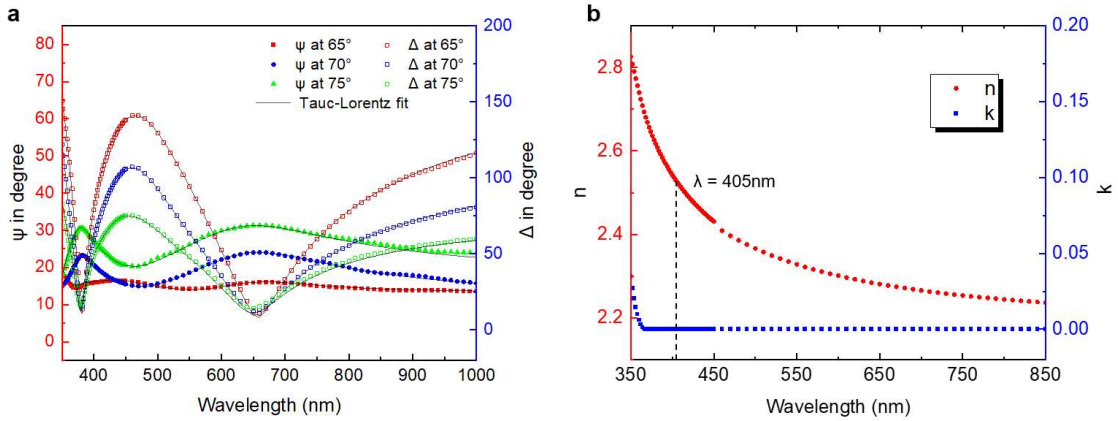

Figure S2. Optical constants fitting and results of TiO_2/Quartz in ellipsometer.

Supplementary Note 2. Simulation model and parameters

The simulated metagrating model is built in COMSOL Multiphysics software and evaluated using numerical finite element method (FEM) (see Figure S3a). The materials' refractive index used in the simulations are: SiO_2: 1.47, TiO_2: 2.6. The boundary conditions at the simulation domain side walls are periodic boundary conditions (Floquet periodicity), and at the bottom and the top are periodic ports, with the bottom port being the incident port. Perfectly Matched Layers (PML) absorbing boundary conditions are applied into the bottom and the top layers. The light source with 405nm wavelength is employed for the simulation. The supercell of metagratings in this work is composed of 9 nanobricks. The sides are chosen in the range of 82 nm to 165nm in order to cover G*2π phase shift (see Figure S3b). Round corners with 30 nm radius are included in this design considering the fabrication limitation of lithography.

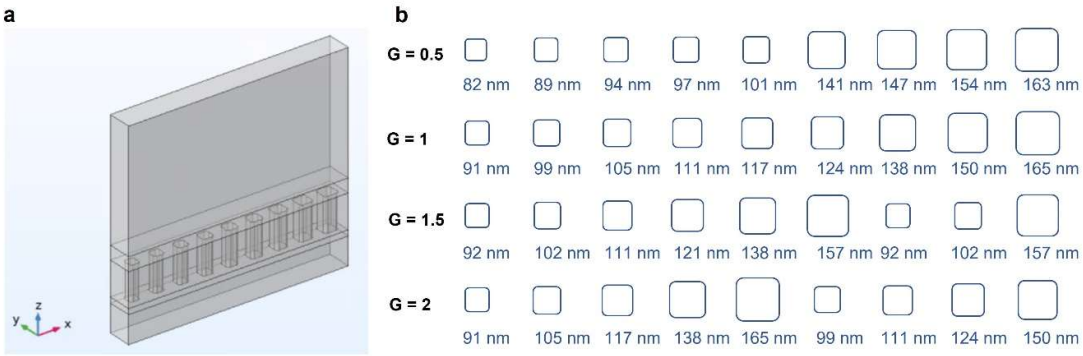

Figure S3. (a) Simulation model in Comsol Multiphysics. (b) The nanobrick sides after optimization for four cases: G = 0.5, 1, 1.5, 2.

The simulated diffraction distribution in the range of G = 0 to 1 is shown in Figure S4. 71% beam has been diffracted into the 0^{th} and 1^{st} order, and the diffraction ratio (I_1/I_0) can be controllable as desired in a large range.

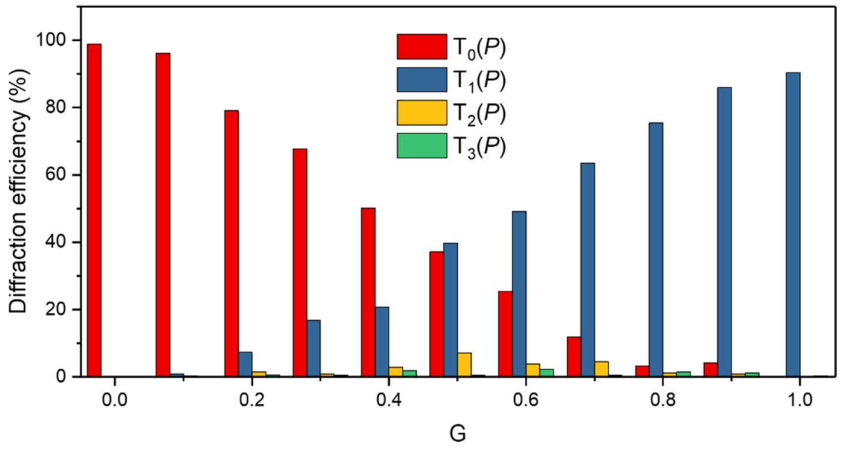

Figure S4. Diffraction efficiency of 0^{th}, 1^{st}, 2^{nd},3^{rd} modes in the range of G = 0 to 1.

Supplementary Note 3. Measurement of diffraction angle

In our experiment, the deflection angle can be decided by recording the distance between the high order diffractive spot and non-diffractive transmittance spot (d_1 and d_2 for 1^{st} and 2^{nd} order) on imaging screen when the screen is fixed away from the grating with a certain distance D (see Figure S5a). Then the diffraction angel can be derived $\theta_i = \arctan(d_i/D)$, where i represents the diffraction order. The practical experimental setup is shown in Figure S5b. Figure S5c shows the measured D in the setup. Figure S5d denotes the position of 0^{th} order beam when the incident beam only passing through the transmissive substrate, no diffraction happens. Figure S5e shows the projection diffraction beams on the screen. The measured d_i is shown in table S2 when D is fixed at 6 cm. The calculated angles in this measurement are 9.46, 19.29, 29.54°, which is in good agreement ($\Delta = |\theta - \theta t| < 0.5°$) with the theoretical values. The little deviation is caused by the distance measurement error in the free-space setup.

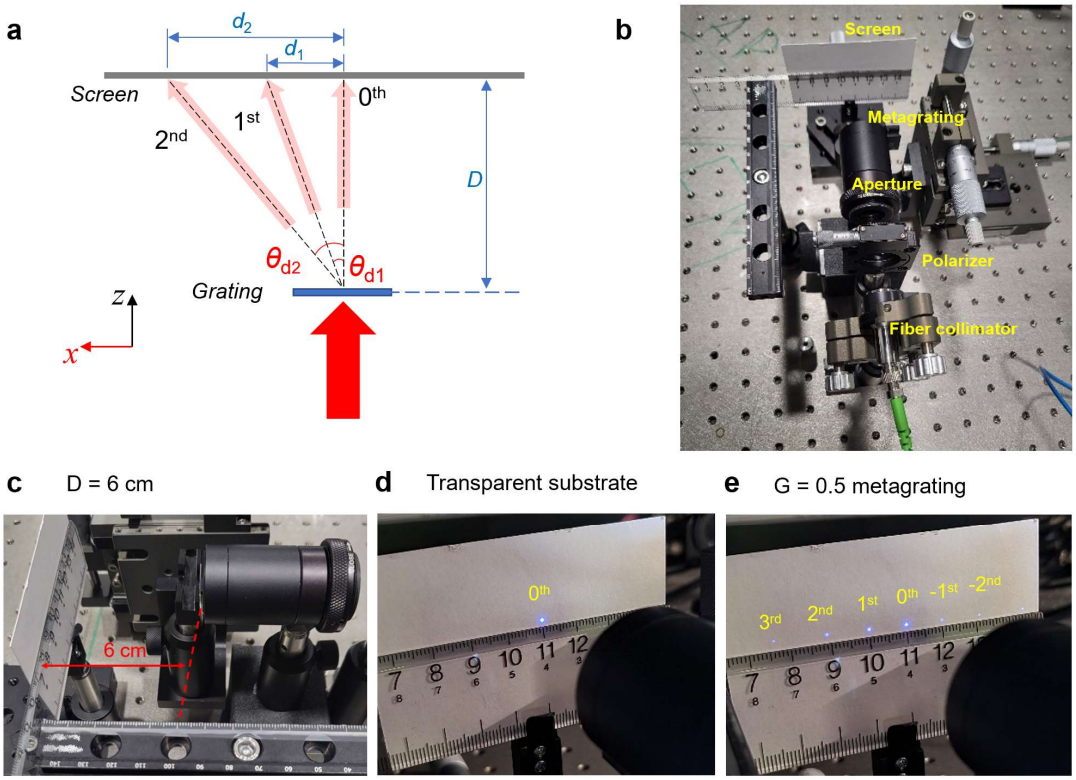

Figure S5. Diffraction angle measurement. a) Scheme of measurement, where D is the distance between screen and metagrating, d is the distance between the projections of high-order diffraction spot and 0^{th} spot, θ represnts the diffraction angle; b) Layout of experiment setup. The projection image on screen of incident laser after passing through c) transparent substrate (quartz) and d) the metagrating with G = 0.5.

Table S2.

D = 6cm	3rd	2nd	1st	0th	-1st	-2nd
d (cm)	3.4	2.1	1	0	1	2.1
θ (°)	29.54	19.29	9.46	0	9.46	19.29
θt (°)	30	19.47	9.59	0	9.59	19.47

Supplementary Note 4. Optical imaging of metagrating

The optical images of metagratings are showed in Fig. S6. Four gratings have the same period, corresponding to the distance between the thick fringes. In the cases of G = 1.5 and 2, sub-fringes emerge inside the main period which indicated the 2π phase jump in each supercell.

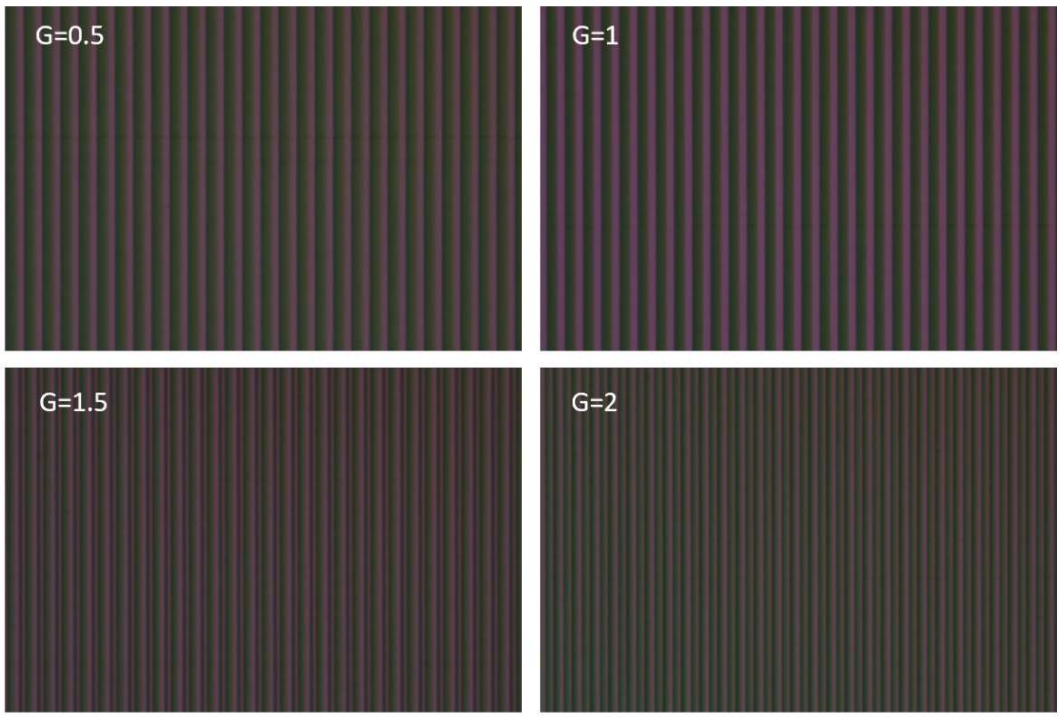

Figure S6. The microscopy of gratings with G factors of (a) 0.5, (b) 1, (c) 1.5, and (d) 2. The background color casts come from unoptimized white balance of microscopy.

Supplementary Note 5. Diffraction intensity profile measured by CCD

Since the large difference of the intensity distribution between diffraction orders, recording them with same settings suffers from the issue of over-exposure (see Fig. 6a,b). To capture the clear profiles of each order, we use shorter exposure time for the brighter diffracted spot. This method is valid due to the linear relation between the recorded intensity profiles and exposure time in the employed CCD camera (Thorlabs DCC3260M). Fig. S6a shows the captured profiles of one light spot respectively with 10-50ms camera exposure times, where longer exposure time corresponds to larger signal and background noise. If we define a factor as the ratio between different exposure time, then the influence of different exposure time can be excluded by dividing this factor. Here we normalized the intensity profiles to 10 ms exposure time, therefore the factors for 20, 30, 40, 50 ms exposure time cases are respectively 2, 3, 4, 5. After normalization, all the profiles are unified as shown in Fig. S4b, which demonstrates the effectiveness of the methodology employed to solve the over-exposure here.

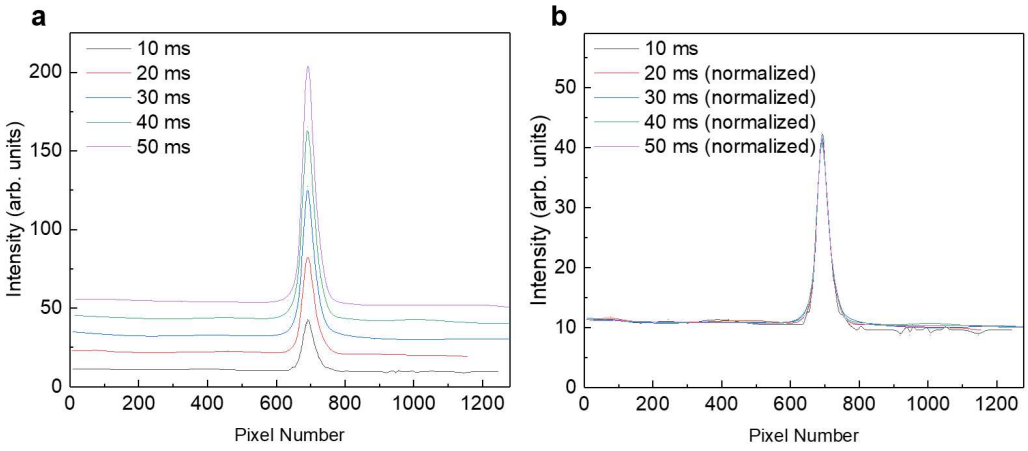

Figure S7. a) The intensity of one light spot measured with a set of exposure time of the CCD. b) After normalization of exposure time, the spot intensity profiles are unified.

Supplementary Note 6. Diffraction with oblique incidence

Varying the incidence angle of the beam adds additional degrees of freedom for manipulating the directions of the diffractive multi-channels as well as the intensity distribution. For convenience, we fabricated four gratings on one substrate and tilted the metagratings instead of tilting beam. We define the sign of tilting angle positive when to the initial blazing direction (dominant diffraction orders), and negative when opposite to the blazing direction. Four tilting angles of $\pm 7.5°$ and $\pm 15°$ were measured (see Fig. S8). According to Eq. (1), the positive tilting tends to decrease the diffraction angles of dominant orders, while negative tilting oppositely increases the angles (Table S3).

Figure S8. Measure scheme for tilting metagrating respectively at cases of ±7.5° and ±15°.

Table S3. The calculated diffraction directions of a set of orders dependent on different metagrating tilting angles.

Diffraction order / Tilting angle	-3rd	-2nd	-1st	0th	+1st	+2nd	+3rd
-15°	-28.96°	-19.27°	-9.71°	0°	10.18°	21.31°	34.36°
-7.5°	-29.18°	-19.20°	-9.57°	0°	9.79°	20.14°	31.59°
0°	-30°	-19.47°	-9.59°	0°	9.59°	19.47°	30°
7.5°	-31.59°	-20.14°	-9.79°	0°	9.57°	19.20°	29.18°
15°	-34.36°	-21.31°	-10.18°	0°	9.71°	19.27°	28.96°

Simultaneously, the slanted device imparts the beam with linear pre-set phase when reaching the grating. It means that the transmitted wavefront combines both the pre-set phase and the grating elements retardation, which equals to increasing/reducing the G factor if the pre-set phase adds/compensates to the initial grating retardation. As a result, the intensity reconstruction happens, see Fig. S9.

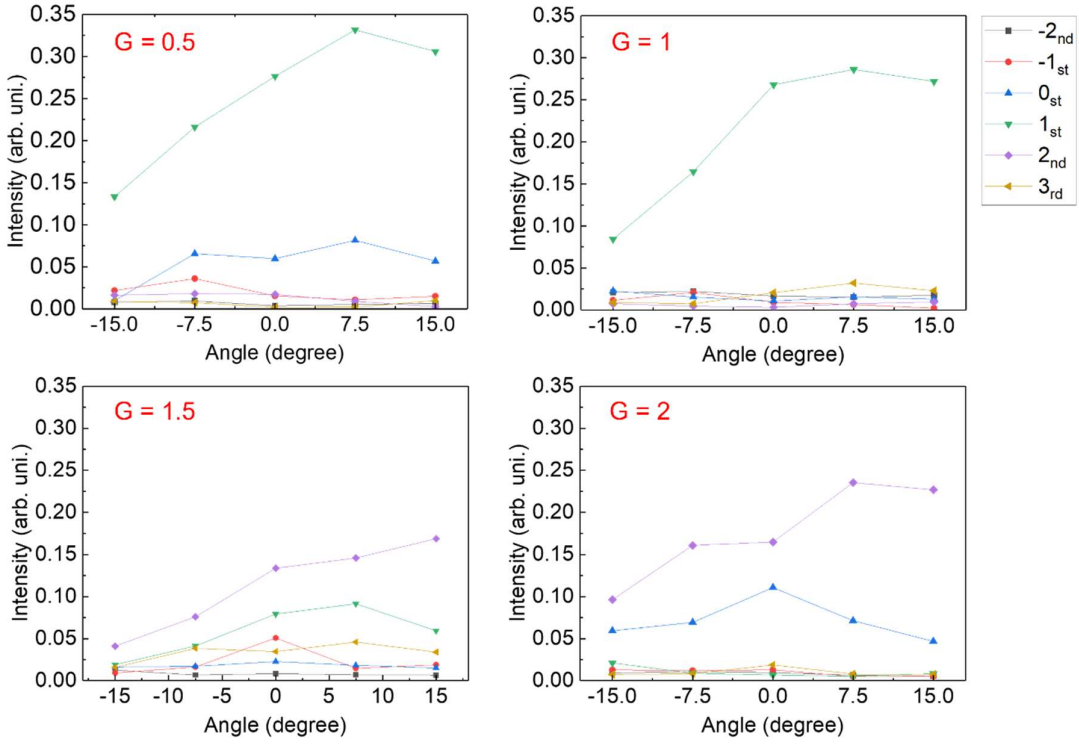

Figure S9. The intensity distribution of diffractive orders in four metagratings (with G = 0.5, 1, 1.5, 2) measured by *P* polarized laser with different oblique incidence angles.

Supplementary Note 7. Diffraction with wavelength variation

On the other hand, tuning the laser wavelength from λ_0 to λ' can similarly change not only the diffraction angles but also the effective G factor:

$$G' = (n'/n_0)\frac{\lambda_0}{\lambda'}\, G,$$

where n_0 and n' are the refractive index of TiO_2 at the wavelength λ_0 and λ'. The diffraction performances dependent on wavelength are shown in Fig. S10.

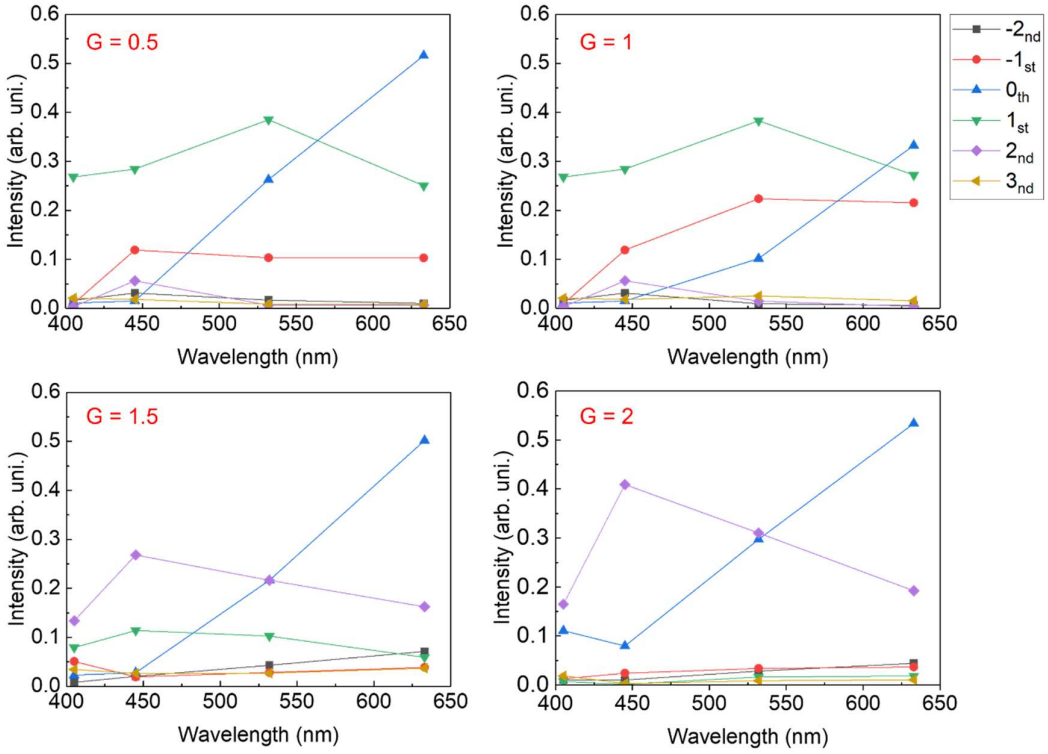

Figure S10. The intensity distribution of different diffractive orders in four metagratings (with G = 0.5, 1, 1.5, 2) measured by *P* polarized laser with different wavelengths.

Supplementary Note 8. Bifocal incomplete phase metalens

The concept of incomplete phase can be extended to other metasurface designs such as polarization insensitive bifocal metalens. A focusing metalens can be viewed as the concatenation of multiple concentric belts, where every belt covers 2π phase shift along the radial direction so that the incident light is directed to the first diffraction orders, which eventually converge at the focal point. If each belt covers 2πG phase change where G is not necessarily an integer, then the incident light will be directed into 2 diffraction orders and subsequently converge at 2 focal points. To illustrate this design concept, metalens designs

with G = 1 (conventional metalens design) and G = 1.5 are simulated. Instead, circular nanopillars are employed considering 360° full symmetric feature of lens on the focus plane (see Figure S11). All nanopillars are 415 nm high with dimeter from 95 to 175nm, and they are arranged in concentric circles with each circle made up of identical nanopillars (see Figure S12 a,b).

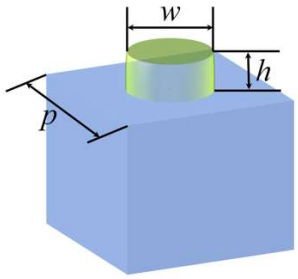

p (nm)	*h* (nm)	*w* (nm)							
270	415	95	104	115	124	130	148	158	175

Figure S11. Nanopillar dimension used for metalens design, where *p* represents the pitch, *w* and *h* is the diameter and height of the pillar.

For a given focal length, the metalens is divided into a series of concentric belts. In each belt, the phase change along radial direction is 2π (G = 1) or 3π (G = 1.5). The radius, height and spacing of the nanopillars are optimized to imprint the desired 2πG phase in each belt, indicated by the black curves at the middle position.

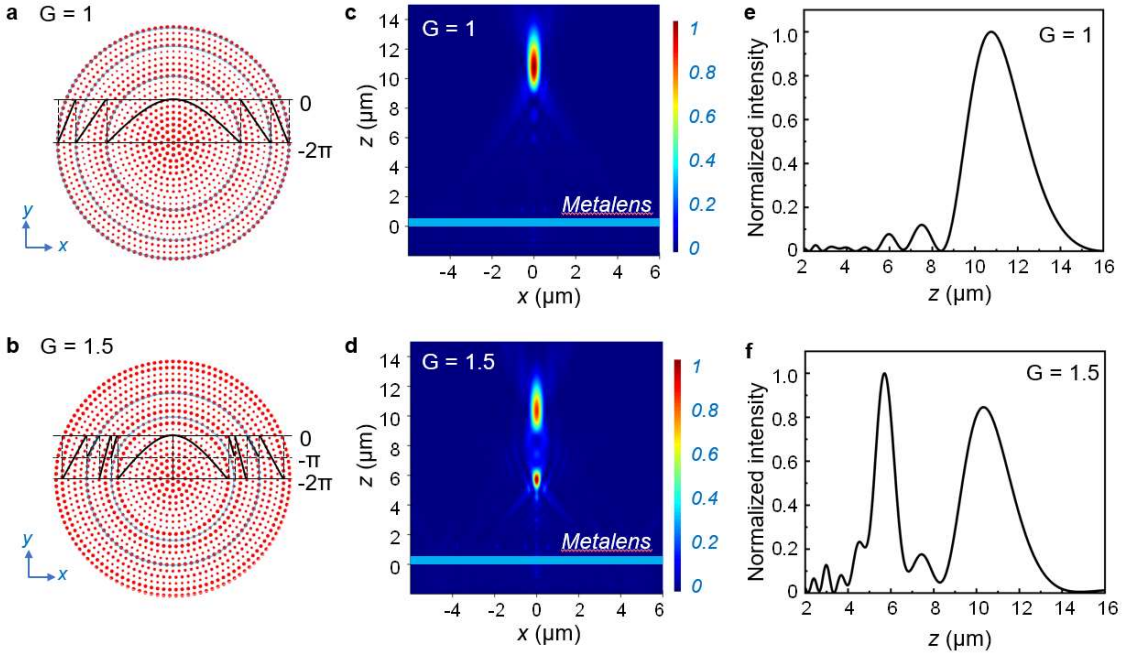

Figure S12. a,b) The nanostructures and phase profiles (middle black lines) of metalens with G = 1 and G = 1.5, respectively. c,d) Power distribution of the focal point at the *xz* plane of two metalens with G = 1 and G = 1.5, respectively. e,f) are respectively the focal spots intensity profiles along *z* direction at the center position ($x = y = 0$).

In both designs, the incident plane wave is propagating along the *z* axis. After passing through the metalens devices, the wavefront is modulated and converged into bright focal points as shown in the *xz* cross-section plots (Figure S12c, d). For G = 1, only one focal point is produced at z = 11 μm, which stems from the constructive superposition of the 1st diffraction of radially repeated meta-atoms. The calculated efficiency of this focus is 72.25%. Notably, when G = 1.5, *i.e.,* the total phase change in each section is 3π, the other bright focal spot emerges at around z = 5.5 μm due to the convergence of the 2nd diffraction order. Both foci have high brightness, with the calculated efficiencies of 33.22% and 17.12%, respectively. Comparing to those bifocal metalens designed with multiplexing scheme, the efficiencies of the two foci are high regardless of the incidence polarizations because all the incident beams contribute to each focus. The intensity profiles of foci along *z*-axis ($x = y = 0$) are given in Figure S12e, f.